Controllable synthesis of nickel nanowires and its application in high sensitivity, stretchable strain sensor for body motion sensing

Shan Wang,[a] Kaifeng Chen,[a] Min Wang,[a] Haosheng Li,[a] Guorui Chen,[a] Jian Liu,[a] Luhang Xu,[a] Yue Jian,[a] Chengda Meng,[a] Xiaoyi Zheng,[a] Suyu Liu,[a] Chong Yin,[a] Zongrong Wang,[*a] Piyi Du,[*a] Shaoxing Qu[*b] and Chi Wah Leung[*c]

a State Key Lab of Silicon Materials, School of Materials Science and Engineering, Zhejiang University, Hangzhou, Zhejiang Province, China

E-mail: zrw@zju.edu.cn, dupy@zju.edu.cn

b Key Laboratory of Soft Machines and Smart Devices of Zhejiang Province, Zhejiang University, Hangzhou 310027, China

E-mail: squ@zju.edu.cn

c Department of Applied Physics, The Hong Kong Polytechnic University, Hung Hom, Hong Kong, China

E-mail: apleung@polyu.edu.hk

Abstract: A facile, low-cost magnetic field-assisted chemical reduction method was proposed for synthesizing nickel nanowires (NiNWs) with both controllable diameter and high length to diameter (L/D) ratio at temperature as low as 60 °C. NiNWs with diameter as low as 180 ± 21 nm and L/D ratio as high as 300 were achieved by controlling the reaction temperature, NiCl2 concentration and the quantity of reductant in a magnetic field of 170 mT. Based on the NiNWs, a high-sensitivity and stretchable strain sensor with sandwich structure consisting of NiNWs and Ecoflex elastomer was proposed. Gauge factor as high as 200 was demonstrated up to a strain of 100%. Applications of the sensor in detecting body motion including finger gestures, facial expressions and different phonations are presented. This study provides a promising solution for smart sensors for next generation robotics as well as for human–machine interfacing applications.

Introduction

Flexible sensors have significant importance in many applications such as artificial intelligence (AI), next-generation robots, wearable medical monitoring devices and human motion sensing.1–6 In particular, the rapid development of artificial intelligence requires high-sensitivity sensors to facilitate communication between human users and robots. The robot named Sophia made her debut in Future Investment Initiative and she is the first robot in the world that has been issued identification.7,8 This indicates that robots will become closer to human beings and particularly better company to disabled or elderly people living alone. However, even though Sophia can make some facial expressions, the body cannot move as smoothly as humans. In this case, a high-performance strain sensor can enhance robot performance by detecting minute deformations such as facial expressions or to instruct the robots to conduct specific movements. All these tasks require high sensitivity and stretchability till tensile strain as high as 60%, which is the limit of reversible human skin strain, is achieved.9,10

In recent years, many researchers proposed stretchable strain sensors by embedding conductive fillers (including Ag nanoparticles (AgNPs),11 Ag nanowires (AgNWs),12,13 carbon black,14 graphene,15–18 and carbon nanotube (CNT)19,20) in soft elastomeric materials such as polydimethylsiloxane (PDMS). Morteza et al. fabricated a flexible strain sensor based on a sandwich-structured nanocomposite by embedding AgNWs between two layers of PDMS.13 This device could detect tensile strain since the conductive AgNWs network separates and the resistance increases when the device is stretched; also, a very high stretchability up to 60% was achieved. However, with a gauge factor (GF) of only 4.7, the device might not be sensitive enough to detect the small strains induced by subtle human expressions such as winking or smiling.

Carbon materials are the most common alternatives for preparing strain sensors owing to the outstanding mechanical and electrical properties.21 Sun et al. reported a piezopotential-powered active matrix strain sensor array using a combination of

piezoelectric nanogenerators and coplanar-gate graphene transistors. The strain sensor exhibited very high sensitivity (GF = 389),17 but low stretchability (maximum strain $\varepsilon = 0.3\%$) due to the brittleness of the graphene sheets. Until now, few strain sensors could achieve high sensitivity and stretchability at high strain with low cost, and the reported state of art sensors are shown in Table 1. From the table, one can conclude that sensitivity and stretchability are jointly determined by the elongation ratio of the matrix before breakage and the L/D ratio of the conductive filler. Matrices with high elongation ensure higher sustainable strains and the L/D ratio helps maintain the continuity and stability of the conducting network rather than breaking down and failing upon application of high strain. We can therefore conclude that matrices with better elongation and fillers with high L/D ratio are two prerequisites for high performance strain sensors.

Ecoflex is a member of the hyperelastic elastomer family, which shows elongation higher than 900% before breakage.22 In addition, it has a Young modulus of only 125 kPa,23 which matches well with that of the human epidermis (25–220 kPa)24 and is much lower than that of PDMS,25 making it a promising candidate for application in human–machine interactions.

For conductive fillers, NiNWs were used as conductive materials, the L/D ratio of which were controlled and reached 300 in this study, leading to high stability of the sensors even under large strain. Theoretically, NiNWs with lower L/D ratio have more junctions or contact points to form complete electrical conductive paths of the same length than that by higher L/D ratio. However, these contact points are the weakest parts in the entire conductive path when subjected to tensile strain. With fewer contact points, the conductive path constructed by NiNWs with higher L/D ratio is less likely to be broken, leading to good stability of the sensor even with large strain. Second, since the NiNWs synthesized in this study demonstrate a bead chain rather than smooth and uniform morphology, NiNWs interlock with each other in the neck sites and the conductive network is not easily broken down, leading to good stability and reversibility of the device. Third, due to the magnetic dipole–dipole interactions

between the two ends of the adjacent NiNWs,26,27 conductive paths can be reconstructed, in contrast to sensors with non-magnetic conductive fillers, thus contributing to good performance of the device. Finally, NiNWs are more cost effective than AgNWs and many other conductors, and possess significantly higher intrinsic electrical conductivity ($\sigma Ni = 1.43 \times 105$ S cm^{-1}),28 chemical stability and oxidation resistance.

Herein, we propose a facile low-cost approach to synthesize NiNWs with very high L/D ratio (300) by the magnetic field-assisted chemical reduction method. We embedded NiNWs film between two layers of Ecoflex to fabricate a highly stretchable, sensitive and reliable strain sensor, which could detect the strain induced from finger movements and eye winking, as well as the strain caused by different phonations. Maximum strain of 100% was achieved and the GF (200) was much higher than those of conventional strain sensors.

Experimental

Synthesis of NiNWs

$NiCl_2 \cdot 6H_2O$ was dissolved in a mixed solution of 30 mL deionized (DI) water and 37.5 mL ethanol and stirred for 30 min to obtain a light green solution. Then, 5 mol L^{-1} NaOH solution was added dropwise until the pH of the mixed solution reached 14. The mixed solution was placed in an applied magnetic field of 170 mT at 60 °C and 40 mL hydrazine hydrated solution (85 wt%) was added as the reducing agent. After reacting for 15 min, a black gray solid was formed, which floated on the surface of the solution. The product was collected using an external magnet and was washed by DI water and ethanol several times, in sequence, to remove the byproducts. Finally, the product was dried in vacuum at 120 °C for 6 h.

Fabrication of NiNWs-based sandwich strain sensor

NiNWs were first dispersed in ethanol by sonication and then poured onto a filter paper. Then, a NiNWs membrane was prepared via vacuum filtration and tailored to a small rectangular piece. To prepare the Ecoflex layers, a glass slide was first treated

by UV–ozone and then deposited with trichloro(1H,1H,2H,2H-perfluorooctyl)silane by vacuum vapor technology to facilitate the release of the Ecoflex® 00-30. Ecoflex was obtained by mixing the A and B components in equal weights and degassing for 10 min under vacuum at room temperature. The mixture was deposited on top of pretreated glass slides and cured at 60 °C for 30 min. Following this, the as-prepared NiNWs membrane was transferred onto the Ecoflex substrate. Carbon tapes were attached to two ends of the NiNWs film by silver paste after peeling the membrane off the glass substrate. Finally, another layer of Ecoflex was cast on the surface and cured at 60 °C for 30 min to complete the encapsulation.

Characterization

X-ray diffraction (XRD) of NiNWs was recorded using Cu Kα radiation (λ = 1.5418 Å). SEM (Hitachi S4800, Japan) and TEM (PHILIPS CM200) were used to analyze the morphologies of the NiNWs. The electromechanical properties of the sensors were measured using a Keithley 2602 source meter driven by the LabVIEW program.

Results and discussion

SEM images of NiNWs are shown in Fig. 1(a). Twenty individual nanowires in Fig. 1(a) were evaluated to obtain the average length of 56.3 ± 9 μm. From the inset of Fig. 1(a), it can be seen that the wire diameter is 180 ± 21 nm and the corresponding L/D ratio is 312. Fig. 1(b) shows the XRD pattern of the as-synthesized NiNWs. The peaks at 44.7°, 52.0° and 76.6° correspond to the (111), (200) and (220) crystal planes of Ni, which match the face-centered cubic (FCC) Ni (JCPDS 04-0850, space group, Fm3m (225)). The inset picture shows that the NiNWs were dispersed well in ethanol and could be collected easily by an external magnet. As shown in Fig. 1(c), the selected area electron diffraction (SAED) measurement carried out on a single NiNW consists of diffraction rings, indicating that the NiNW is polycrystalline with FCC structure, which is in agreement with the XRD results. To better understand the synthesis mechanism and the structure of NiNWs, TEM measurements were carried out and the results are shown in Fig. 1(d). The results indicate that NiNWs possess a

bead chain morphology formed by a string of closely aligned nickel nanoparticles under the magnetic field.

The mechanism of NiNWs synthesis by hydrazine hydrate

First, Ni2+ and OH− form Ni(OH)2 owing to the addition of NaOH. Then, Ni2+ is reduced to Ni nuclei by N2H4 in solution. Stable Ni nuclei are formed and further grow to Ni particles. These Ni particles are magnetized by the external magnetic field and connect with each other (head to tail) to form NiNWs along the magnetic field direction owing to magnetic dipole interactions. Newly formed Ni particles would connect to the wires at the ends, increasing the lengths of wires. Then, there would be more Ni particles generated that covered the surfaces of NiNWs, which increased the diameters of NiNWs.

NiNWs are formed through the following reactions:

$$Ni2+ + 2OH- \rightarrow Ni(OH)2$$

$$2Ni(OH)2 + N2H4 \rightarrow 2Ni + N2 + 4H2O$$

The overall reaction is

$$2Ni2+ + N2H4 + 4OH- \rightarrow 2Ni + N2 + 4H2O$$

The effect of reaction time

To figure out the growth process of NiNWs in detail and to verify the synthesis mechanism, three samples were collected at different reaction times. The schematic diagrams of the NiNWs formation process and the corresponding SEM images of samples collected at 7, 10 and 15 min are shown in Fig. 2. First, Ni(OH)2 is generated from Ni2+ owing to the addition of NaOH and is reduced to Ni nuclei to further form Ni particles by reduction by hydrazine hydrate. At this stage, the reduced Ni exists mainly in the form of particles (Fig. 2(a)). As the reaction continues, the particles are lined up and packed together to form strings along the magnetic field (Fig. 2(b)). Moreover, newly-generated particles continue to join at the ends of the strings owing

to magnetic dipole interactions to form wires. In this case, particles and wires co-exist. At the 15 min stage (Fig. 2(c)), straight and uniform nanowires with bead chain morphologies were formed under magnetic field.

The effect of magnetic field

The effect of external magnetic field on NiNWs synthesis is shown in the SEM images of Fig. 3. In the absence of an external field (Fig. 3(a)), Ni particles connect to form curved and short wires, but some particles are still isolated. For the sample with the magnetic field applied during preparation (Fig. 3(b)), Ni particles are magnetized under the applied magnetic field and are held together along the magnetic field. In addition, the short wires could connect with each other head to tail to form long wires because of magnetic dipole interactions. Hence, as shown in Fig. 3(b), NiNWs synthesized under magnetic field are straight and long with average diameter of 180 nm.

The effect of hydrazine hydrate

$NiCl_2$ solution is transparent with light green color, which turns turbid green after mixing with NaOH. The solution changes to dark gray and forms fluffy solids when hydrazine hydrate is added, indicating the formation of Ni particles.

To illustrate the role of hydrazine hydrate as a reductant, different concentrations of hydrazine hydrate (0.88 mol L^{-1}, 1.68 mol L^{-1}, 5.56 mol L^{-1} and 7.66 mol L^{-1}) were added to the mixed solution of $NiCl_2$ and NaOH for investigation. As shown in Fig. 4(a), when the concentration of hydrazine hydrate is only 0.88 mol L^{-1}, Ni^{2+} is reduced and aggregated to form irregular and small Ni particles. Fig. 4(b) shows that with on increasing the amount of hydrazine hydrate, the small particles tend to grow to regular spherical particles. Since the reductant quantity is limited, only part of the $Ni(OH)_2$ is reduced to Ni particles and these particles form comparatively short wires under the external magnetic field. With 5.56 mol L^{-1} hydrazine hydrate (Fig. 4(c)), Ni particles continue to be generated and connect with each other under magnetic field to form long wires with several isolated Ni particles still present around the wires. As the

concentration of hydrazine hydrate reaches 7.66 mol L^{-1}, no particles can be observed and the wires become long and more uniform (Fig. 4(d)).

The effect of $NiCl_2 \cdot 6H_2O$ concentration

Fig. 5(a–f) display the SEM images of six samples synthesized with different concentrations of $NiCl_2 \cdot 6H_2O$: 0.003 mol L^{-1}, 0.006 mol L^{-1}, 0.01 mol L^{-1}, 0.02 mol L^{-1}, 0.03 mol L^{-1} and 0.04 mol L^{-1}. As shown in Fig. 5(a), the products are Ni nanoparticles because the amount of Ni^{2+} was not enough to form wires with the concentration of $NiCl_2 \cdot 6H_2O$ being 0.003 mol L^{-1}. As shown in Fig. 5(b), when the concentration increases to 0.006 mol L^{-1}, NiNWs could be observed with average diameter of 180 nm. With an increase in $NiCl_2 \cdot 6H_2O$ concentration, the diameters of NiNWs also increased. The average diameters of NiNWs in (c), (d), (e), and (f) are 211 nm, 234 nm, 520 nm and 608 nm, respectively.

Since high Ni^{2+} concentration leads to high supersaturation, fast nucleation rate could be obtained. A large quantity of Ni nuclei could be formed in a short time. Moreover, Ni particles are more likely to agglomerate as the concentration of Ni^{2+} increases. Small particles aggregate together or form at the surfaces of large particles. In this case, isolated small particles gradually disappear, while large particles increase in size by migration to decrease the energy of the system. Moreover, a high concentration of Ni^{2+} contributes to the growth of Ni particles. Hence, the diameter of NiNWs increases with the concentration of Ni^{2+}.

Furthermore, 20 individual NiNWs (shown in inset images of Fig. 5) were analyzed to obtain the average L/D ratio. The relationships between diameter and L/D ratio of NiNWs with $NiCl_2 \cdot 6H_2O$ concentration are shown in Fig. 6. It is evident that the L/D ratio of NiNWs decreased with an increase in concentration of $NiCl_2 \cdot 6H_2O$. As described in the last paragraph, the NiNWs diameter increases with $NiCl_2 \cdot 6H_2O$ concentration.

Fabrication and characterization of NiNWs/Ecoflex sandwich structured sensor

To evaluate the performance of NiNWs in real applications, a sandwich-structured

strain sensor was fabricated as shown in Fig. 7. NiNWs were dispersed in ethanol and a NiNWs membrane was prepared via vacuum filtration, followed by cutting to a small rectangular specimen. This NiNWs film would be the conductive layer sandwiched between two layers of Ecoflex films. The resistance of the strain sensor increases during stretching and decreases upon releasing the stress. During stretching, the device resistance increases and can be attributed to two aspects. First, some of the NiNWs separate from each other and the loss of contact among NiNWs leads to sharp resistance increase in the strain sensor. At the same time, owing to the bead chain morphology, NiNWs interlock with each other to form a relatively stable conductive network. During stretching, although the distances between NiNWs increase, the conductive network still exists in a sparse state. In this case, the resistance of the sensor increases slightly. The combined effect leads to resistance increase during stretching and leads to high sensitivity of the strain sensor. Furthermore, due to the magnetic dipole–dipole interactions between two ends of adjacent NiNWs,26,27 conductive paths can be reconstructed easily and the conductive network remains stable and reversible, leading to good reversibility and stability of the device. In this case, after releasing the stress, the NiNWs reconnect with each other to reconstruct the conductive path and the resistance returns to the original value.

Furthermore, cycling tests were carried out to evaluate the long-term stability and response time of the strain sensors using an Instron 5943 Materials Testing System and a LabVIEW-controlled Keithley 2602 source meter. The strain sensor was subjected to 2000 cycles of repeated stretching and release (from $\varepsilon = 0\%$ to $\varepsilon = 30\%$). Fig. 9 demonstrates the superior reversibility and stability of the sandwich-structured strain sensor under repeated and continuous stretch and release cycles, which is promising for practical application. The inset images are the current response of the strain sensor after hundreds of cycles. As shown in the images, the device possesses a fast response time of 0.32 s.

The response time, one of the most important parameters for a strain sensor, was further confirmed by subjecting the samples to 30% strain at different frequencies. As

shown in Fig. 10, the sensor is stretched to 30% strain and released by the testing system with frequencies of (a) 1.3 Hz, (b) 2 Hz, (c) 2.7 Hz and (d) 3 Hz. When the loading cycle frequency of the test system is below 2.7 Hz, the response time of the sensor decreases with increasing frequency. However, when the frequency increases to above 2.7 Hz, the response time is unchanged anymore and remains the same of 0.32 s, indicating that 0.32 s is the ultimate response time of the strain sensor. Hence, the shortest response time of the strain sensor is 0.32 s.

The sandwich-structured strain sensor is stretchable, skin mountable and sensitive, making it reliable for sensing human motions and micro expressions in practical applications. As a demonstration, the sensor was fixed on the surface of an index finger and connected to a Keithley 2602 source meter to monitor the finger gestures as shown in Fig. 11. Once the finger is bent, strain is generated and the current through the sensor decreases. In this case, larger degree of sensor bending will lead to greater current decrease. The change of current signals with finger motion was recorded. When the finger is bent slightly and drastically, the current responses are clearly different and can be easily distinguished. With larger degree of bending, higher strain will be generated and thus, the sensor can be used to sense different human finger gestures as shown in Fig. 11(a). Instead of moving back to the flat state, Fig. 11(b) shows continuous responses by holding the finger in a particular bending state for a few seconds.

In addition to the small strain induced by finger bending, large strain can be generated by holding a fist and the corresponding current responses are shown in Fig. 12(a). When the fist is clenched, the NiNWs are separated from each other and the distances among NiNWs would increase, leading to the increase in the resistance. Resistance can return to the original value when the fist is unclenched, demonstrating the potential of the as-fabricated strain sensor for sensing large strains. As shown in Fig. 12(b), the strain sensor can also be used to monitor the micro expressions near the corners of eyes, and the duration of opening and closing of the eye can be clearly identified.

Finally, the sensor was adhered near the mouth to sense different human phonations. Different phonations result in different levels of strain to the sensor, reflected by the measured current in Fig. 13. It can be seen that the sensor is sensitive to different facial expressions during phonation. Moreover, the current of the sensor shows stable and repetitive signals, proving excellent stability and repeatability of the strain sensor in body motion sensing applications.

Conclusion

In summary, NiNWs with controllable diameter and L/D ratio were synthesized by chemical reduction method under external magnetic field. By optimizing the preparation conditions, the diameter of NiNWs decreased to 180 nm and the L/D reached 300 using this method. Based on the investigation of the structures of NiNWs and the influence of synthesis parameters, the synthesis mechanism was discussed. Furthermore, an Ecoflex–NiNWs–Ecoflex sandwich-structured strain sensor was fabricated to sense body motion. The current variation of the sandwich film was sensitive toward distinguishing different finger gestures, phonation and facial expressions. In summary, morphology-controllable NiNWs were synthesized by the induced chemical reduction method and was used to fabricate a sandwich-structured strain sensor that exhibited good sensitivity, stability, and flexibility in body motion sensing.

Conflicts of interest

There are no conflicts of interest to declare.

Acknowledgements

This study was supported by the National Natural Science Foundation of China (Grant numbers 51702285, 51772269, 91748209, 11525210 and 11621062), and the Zhejiang Provincial Natural Science Foundation (Grant number LY17F040003). The authors also want to thank the support of the Open Projects Foundation of Yangtze Optical Fiber and Cable Joint Stock Limited Company (YOFC) (Grant number SKLD1708), 2017-HT-ZD, HKSAR (PolyU 153015/14P) and PolyU (1-ZE25,

1-YBPU).

Figures & Tables

Table 1 Maximum strains and gauge factors of strain sensors

No.	Material	Maximum strain (%)	Gauge factor	Ref no.
1	AgNWs/PDMS	60	4.7	13
2	Graphene/PDMS	100	7.1	16
3	Graphene nanocellulose/PDMS	7.1	15.4	15
4	Carbon paper/PDMS	20	25.3 (0–3%) 4.7 (3–20%)	21
5	Graphene/PVDF-TrFE	0.3	389 (0–0.1) 69 (0.1–0.3)	17
6	AgNWs/PDMS	35	20	12
7	AgNPs/PDMS	25	7	11
8	CNT + PUD/PEDOT:PSS	100	62.7	19
9	Carbon black/PDMS	150	29.1	14
	This work NiNWs/Ecoflex	100	200	

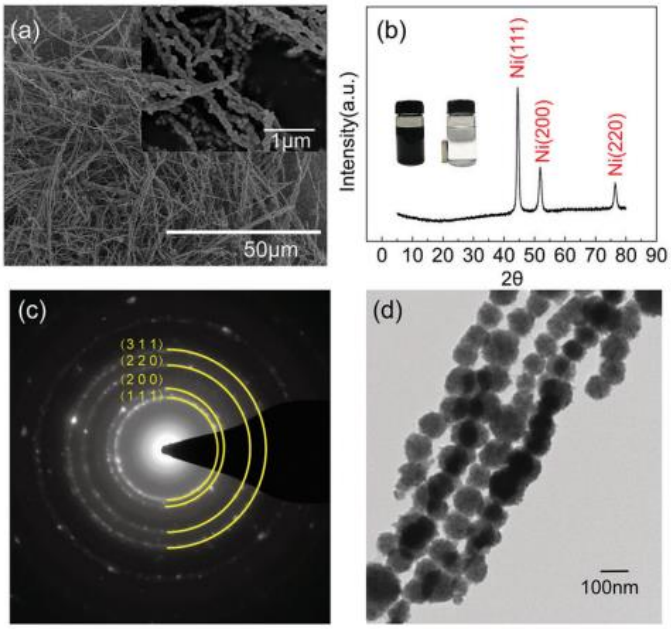

Fig. 1 SEM images (a) and XRD pattern (b) of NiNWs powder. Inset: Photograph of NiNWs solutions with and without external magnetic field. SAED pattern and TEM image of NiNWs are shown in (c and d), respectively.

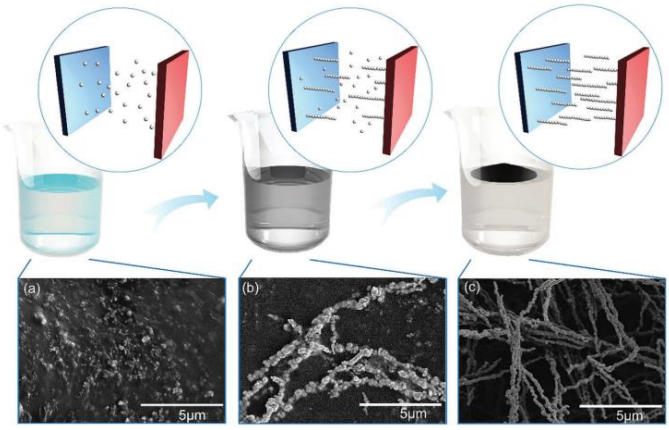

Fig. 2 Schematic illustration (upper panels) and corresponding SEM micrographs (lower panels) of the NiNWs synthesis process at different times (a: 7 min; b: 10 min; c: 15 min).

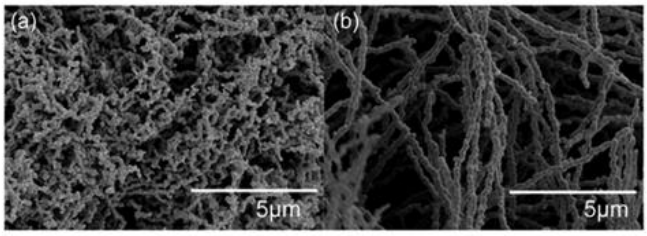

Fig. 3 SEM morphologies of NiNWs synthesized without (a) and with (b) external magnetic field.

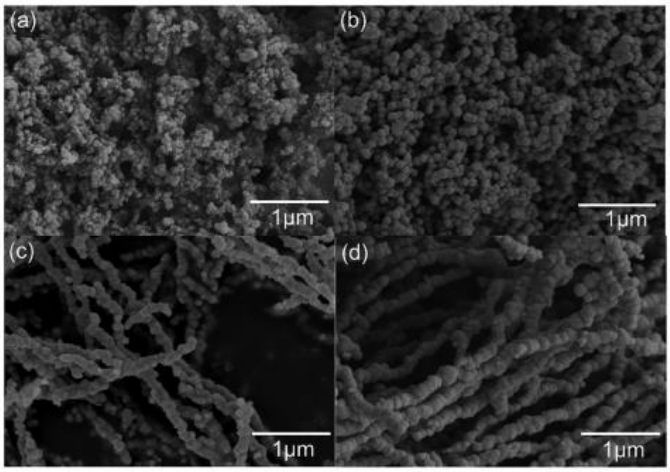

Fig. 4 Variation of NiNWs morphology with the concentration of reductant hydrazine hydrate. (a) 0.88 mol L^{-1}, (b) 1.68 mol L^{-1}, (c) 5.56 mol L^{-1} and (d) 7.66 mol L^{-1}.

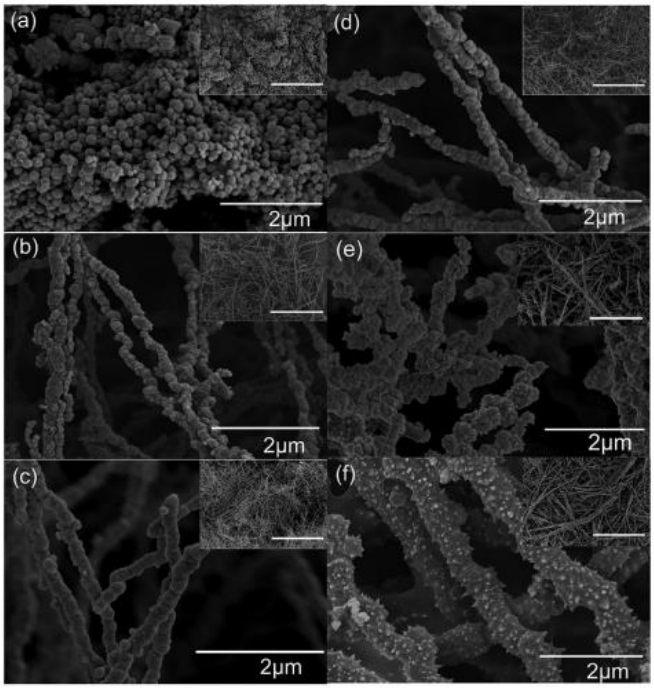

Fig. 5 NiNWs with different concentrations of $NiCl_2 \cdot 6H_2O$: (a) 0.003 mol L^{-1}, (b) 0.006 mol L^{-1}, (c) 0.01 mol L^{-1}, (d) 0.02 mol L^{-1}, (e) 0.03 mol L^{-1}, and (f) 0.04 mol L^{-1}. The scale bar in the insets = 50 μm.

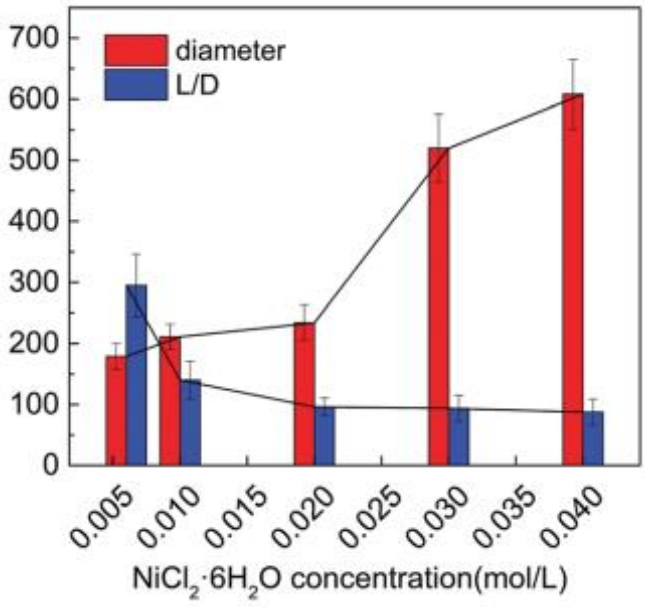

Fig. 6 The diameter and L/D of NiNWs with varying concentration of $NiCl_2 \cdot 6H_2O$.

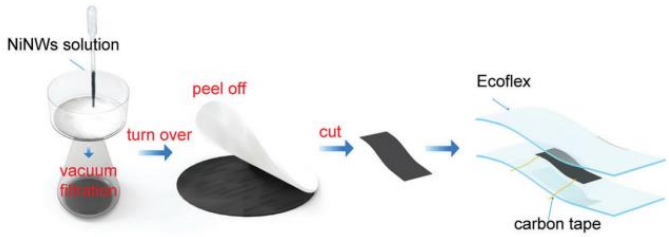

Fig. 7 Schematic diagram for fabricating the sandwich-structured strain sensor.

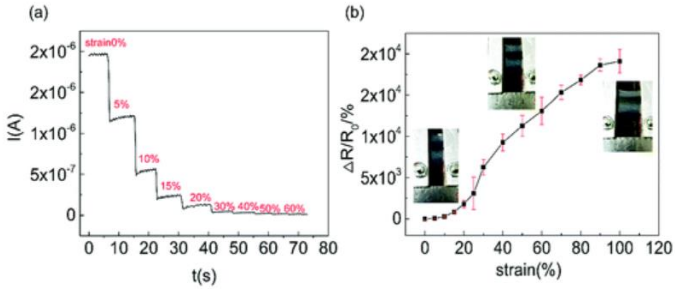

Fig. 8 (a) Response of the sandwich-structured strain sensor upon stretching. (b) Relative change of resistance versus strain for the sensor. Pictures show the sample in different strain states.

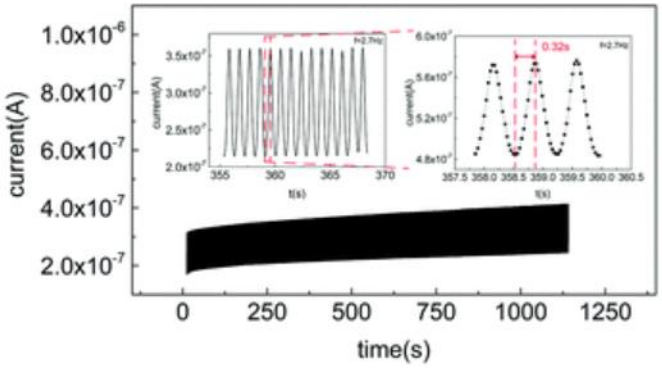

Fig. 9 Current change of the strain sensor under 2000 stretch/release cycles with 30% strain. Insets show the zoomed-in current response and the corresponding response time.

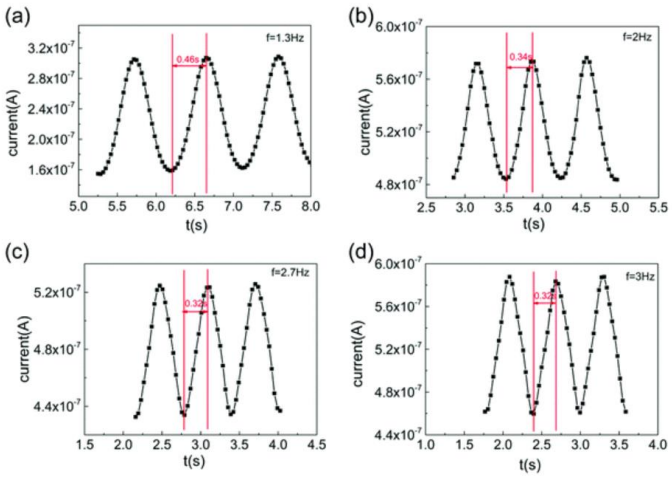

Fig. 10 Response time measurements of the sensor at 30% strain with different loading rates on the Instron 5943 Materials Testing System. (a) f = 1.3 Hz; (b) f = 2 Hz; (c) f = 2.7 Hz; and (d) f = 3 Hz.

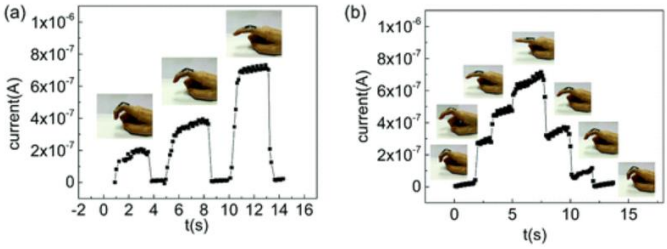

Fig. 11 (a) Current response of the sensor for a finger gesture in bending–flat–bending cycles with different bending radii. (b) Continuous response of the current with continuous finger gesture change.

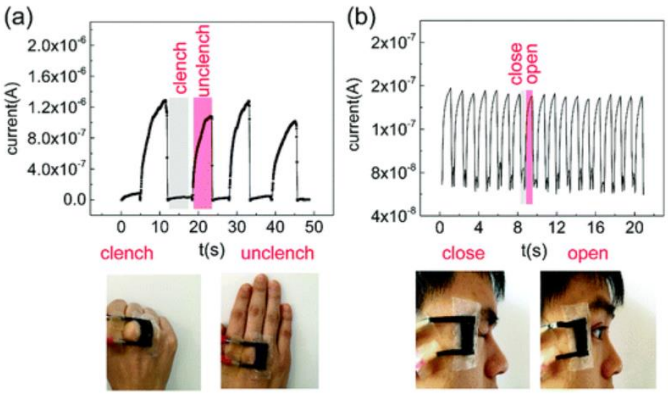

Fig. 12 (a) Current response of the sensor when making a fist. (b) Current response of pressure sensor attached to the corner of eye in open and closed states.

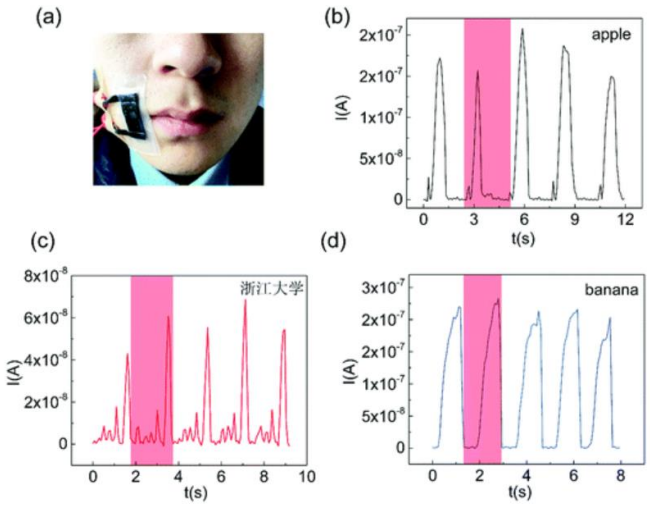

Fig. 13 (a) Photo of the sensor taped on the corner of the mouth. (b–d) Current response of the strain sensor associated with different phonations.

References

1. Z. F. Liu , S. Fang , F. A. Moura , J. N. Ding , N. Jiang , J. Di , M. Zhang , X. Lepró , D. S. Galvão , C. S. Haines , N. Y. Yuan , S. G. Yin , D. W. Lee , R. Wang , H. Y. Wang , W. Lv , C. Dong , R. C. Zhang , M. J. Chen , Q. Yin , Y. T. Chong , R. Zhang , X. Wang , M. D. Lima , R. Ovalle-Robles , D. Qian , H. Lu and R. H. Baughman , Science, 2015, 349 , 400.

2. X. Wang, Z. Liu and T. Zhang, Small, 2017, 13, 1602790.

3. W. Gao, S. Emaminejad, H. Y. Nyein, S. Challa, K. Chen, A. Peck, H. M. Fahad, H. Ota, H. Shiraki and D. Kiriya, Nature, 2016, 529, 509.

4. Y. Khan, A. E. Ostfeld, C. M. Lochner, A. Pierre and A. C. Arias, Adv. Mater., 2016, 28, 4373.

5. Z. Wang, S. Wang, J. Zeng, X. Ren, A. J. Chee, B. Y. Yiu, W. C. Chung, Y. Yang, A. C. Yu, R. C. Roberts, A. C. Tsang, K. W. Chow and P. K. Chan, Small, 2016, 12, 3827.

6. F. Han, J. Li, S. Zhao, Y. Zhang, W. Huang, G. Zhang, R. Sun and C. P. Wong, J. Mater. Chem. C, 2017, 5, 10167.

7. B.Goertzel, J.Mossbridge, E.Monroe, D.Hanson and G.Yu, Humanoid Robots as Agents of Human Consciousness Expansion, 2017.

8. D. F.Hanson, EAP artificial muscle actuators for bio-inspired intelligent social robotics (Conference Presentation), 2017.

9. G. A. Holzapfel Handbook of Materials Behavior Models, 2001, p. 1057.

10. A. Rita Domingues, S. Marreiros, J. Martins, M. Silva and D. Newman, Skin Strain Field Analysis of the Human Ankle Joint, 2010.

11. J. Lee, S. Kim, J. Lee, D. Yang, B. C. Park, S. Ryu and I. Park, Nanoscale, 2014, 6, 11932.

12. K. K. Kim, S. Hong, H. M. Cho, J. Lee, Y. D. Suh, J. Ham and S. H. Ko, Nano

Lett., 2015, 15, 5240.

13. M. Amjadi, A. Pichitpajongkit, S. Lee, S. Ryu and I. Park, ACS Nano, 2014, 8, 5154.

14. N. Lu, C. Lu, S. Yang and J. Rogers, Adv. Funct. Mater., 2012, 22, 4044.

15. C. Yan, J. Wang, W. Kang, M. Cui, X. Wang, C. Y. Foo, K. J. Chee and P. S. Lee, Adv. Mater., 2014, 26, 2022.

16. S.-H. Bae, Y. Lee, B. K. Sharma, H.-J. Lee, J.-H. Kim and J.-H. Ahn, Carbon, 2013, 51, 236.

17. Q. Sun, W. Seung, B. J. Kim, S. Seo, S. W. Kim and J. H. Cho, Adv. Mater., 2015, 27, 3411.

18. Y. Qin, Q. Peng, Y. Ding, Z. Lin, C. Wang, Y. Li, F. Xu, J. Li, Y. Yuan and X. He, ACS Nano, 2015, 9, 8933.

19. E. Roh, B. U. Hwang, D. Kim, B. Y. Kim and N. E. Lee, ACS Nano, 2015, 9, 6252.

20. M. Amjadi, Y. J. Yoon and I. Park, Nanotechnology, 2015, 26, 375501.

21. Y. Li, Y. A. Samad, T. Taha, G. Cai, S.-Y. Fu and K. Liao, ACS Sustainable Chem. Eng., 2016, 4, 4288.

22. S. Ryu, P. Lee, J. B. Chou, R. Xu, R. Zhao, A. J. Hart and S.-G. Kim, ACS Nano, 2015, 9, 5929.

23. R. F. Shepherd, A. A. Stokes, R. M. D. Nunes and G. M. Whitesides, Adv. Mater., 2013, 25, 6709.

24. F. H. Silver, J. W. Freeman and D. Devore, Skin Res. Technol., 2010, 7, 18.

25. Z. Wang, A. A. Volinsky and N. D. Gallant, J. Appl. Polym. Sci., 2015, 131, 547.

26. M. Tanase, L. A. Bauer, A. Hultgren, D. M. Silevitch, L. Sun, D. H. Reich, P. C. Searson and G. J. Meyer, Nano Lett., 2001, 1, 155.

27. X. Xu, G. Friedman, K. D. Humfeld, S. A. Majetich and S. A. Asher, Chem. Mater., 2002, 14, 1249.

28. S. H. Jang, Y. L. Park and H. Yin, Materials, 2016, 9, 239.